




Anisotropic photoelectron emission delay in two-dimensional atomic arrangementsHyosub Park , Youngjae Kim, and J. D. Lee **Department of Emerging Materials Science, DGIST, Daegu 42988, Korea* (Received 15 March 2021; revised 18 May 2021; accepted 7 June 2021; published 15 June 2021)

In two-dimensional semiconductors, the density fluctuation potential created by a screening of the photohole is intrinsically anisotropic because of the infinitely periodic planar arrangements of atoms. Modeling the anisotropic-localized screening with the cylindrical geometry, we investigate the emission delay of the photoelectron from $2s$ and $2p_z$ states of graphene in an angle-resolved mode of the attosecond streaking by solving the time-dependent Schrödinger equation. Strong angle dependencies in absolute emission delays of $2s$ and $2p_z$ states are obtained, from which the effects of the infrared-induced continuum transition are ruled out and those of the anisotropic screening could be solely extracted. Consequently, the anisotropic scattering induces photoelectrons to be emitted with substantial negative delays within small angles (i.e., $\theta \lesssim \theta_c$) from the normal direction to the atomic arrangement, that is, a conical electron emission in a very early stage of the photoemission.

DOI: [10.1103/PhysRevB.103.235135](https://doi.org/10.1103/PhysRevB.103.235135)**I. INTRODUCTION**

Technical developments of the strong field laser make it possible to analyze the motion of an electron in the attosecond time scale, for instance, the electron emission delay during the photoemission. The principle experiment of the photoemission time delay was carried out for a tungsten metal [1]. A relative photoemission delay in an atomic neon was also determined between $2s$ and $2p$ orbitals [2], which builds up the photoemission metrology. On the other hand, pioneering theoretical considerations have been made by Eisenbud, Wigner, and Smith (EWS) more than half a century ago [3–5]. They interpret an energy derivative of the photoelectron phase shift by a short-ranged potential as an emission delay, i.e., the EWS delay. In atoms, the EWS delays induced by the Coulomb potential [6,7], the correlation [8–12], and resonance effect [13,14] are addressed. In solids, the Coulomb-type EWS delay shows an agreement with the experiment in a bulk material [15]. Furthermore, several electronic constituents strongly affect the emission delay including the periodic potential [15–17], collective excitations [18–21], spin contribution [22], and strong Coulomb correlation [23]. Additionally, the continuum transition delay induced by the infrared (IR) probe field has been recently found in the pump-probe measurement [24,25].

Previous studies show that the attosecond dynamics of an electron is sensitive to the electronic environment. Recent studies of the isotropic atomic systems show that the photoemission delay depends on the photoelectron emission angle [26–29] according to the continuum transition induced by the IR streaking field. In this point of view, an atomistic two-dimensional system is interesting. In the system, the photoelectron experiences an anisotropic electronic screening

because of planar arrangements of atoms. This makes the atomic potential cylindrically symmetric, which, in addition to the effects of the aforementioned IR-induced transition, produces an inherent correlation with the spatial motion of the photoelectron and the resultant angle-dependent photoelectron emission delay.

In this paper, we calculate the angle-resolved photoelectron emission delay in a two-dimensional system of graphene by solving the time-dependent Schrödinger equation with a model Hamiltonian incorporating the anisotropic density fluctuation potential with the cylindrical geometry. The anisotropic potential is obtained by the density functional theory (DFT) calculation and further parameterized by the potential depth and the anisotropic screenings along in-plane and out-of-plane directions. Graphene is a perfect single atomic layer, which has a few conceptual merits such as the zero transport delay and the negligible electron interaction. Absolute emission delays of $2s$ and $2p_z$ states of graphene are found to strongly depend on the emission angle, which would stem from the IR-induced transition and the anisotropic photoelectron screening. The effect of the anisotropic photoelectron screening could be isolated by excluding the IR-induced transition in a comparison with the isotropic screening. The anisotropic screening is found to result in a velocity cone with earlier electron emission centering around the normal direction to the atomic plane.

The paper is organized as follows. In Sec. II, we propose a model and formulation for the streaking photoemission in a two-dimensional atomic arrangement of graphene. In Sec. III, we provide a calculation of angle-dependent photoelectron emission delays with respect to screening parameters and investigate the origins of their angle dependencies. Among those, we further try to isolate and discuss the effect of the anisotropic potential. Finally, in Sec. IV, we provide a summary and conclusion.

*Corresponding author: jdlee@dgist.ac.kr

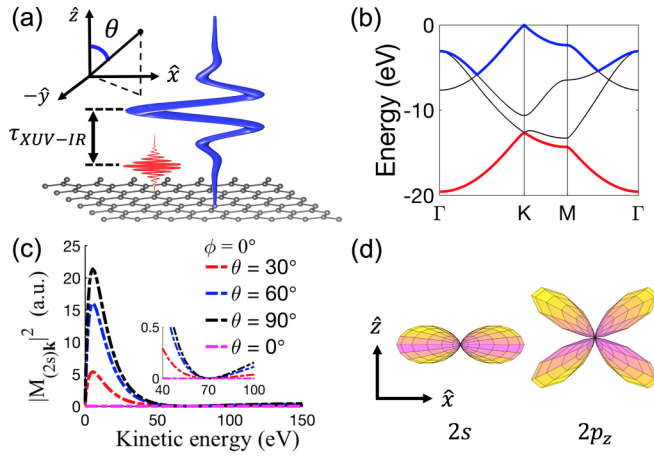


FIG. 1. (a) Schematic view of the streaking photoemission. The \hat{x} -polarized pump (red) and probe (blue) pulses are considered onto graphene. (b) Band structure of the graphene; $2s$ and $2p_z$ bands are drawn in red and blue solid lines. (c) $|M_{Lk}|^2$ for $2s$ and $2p_z$ states with the \hat{x} -polarized XUV pump pulse. (d) Schematics of photoelectron waves excited by the dipole operator from $2s$ and $2p_z$ states.

II. MODEL AND FORMULATION

We propose a single electron model Hamiltonian for a calculation of the attosecond photoelectron streaking in a velocity gauge [23,30,31], whose physical situation is described by a schematic of Fig. 1(a),

$$\begin{aligned} \mathcal{H} = & \varepsilon_L c_L^\dagger c_L + \sum_{\mathbf{k}} [\varepsilon_{\mathbf{k}} - \mathbf{k} \cdot \mathbf{A}_{\text{IR}}(\tau + \tau_{\text{XUV-IR}})] c_{\mathbf{k}}^\dagger c_{\mathbf{k}} \\ & + A_{\text{XUV}}(\tau) \sum_{\mathbf{k}} [M_{Lk} c_L^\dagger c_{\mathbf{k}} + M_{Lk}^* c_{\mathbf{k}}^\dagger c_L] + \sum_{\mathbf{k}\mathbf{k}'} V_{\mathbf{k}\mathbf{k}'} c_{\mathbf{k}}^\dagger c_{\mathbf{k}'}; \end{aligned} \quad (1)$$

c_L^\dagger or c_L is an operator of the target electron with its energy ε_L . We consider two band states of graphene, i.e., the lowest σ band [red line in Fig. 1(b)] and the π band [blue line in Fig. 1(b)] dominantly characterized by $2s$ and $2p_z$ states, respectively. Their energies are given by $\varepsilon_{2s} = -21.6$ eV and $\varepsilon_{2p_z} = -6.6$ eV. A d -state contribution to the π band is ignored [32]; $c_{\mathbf{k}}^\dagger$ or $c_{\mathbf{k}}$ is an operator of the photoelectron and its kinetic energy $\varepsilon_{\mathbf{k}} = \mathbf{k}^2/2$. The second term of Eq. (1) is for the photoelectron streaking employing the \hat{x} -polarized IR probe pulse [i.e., $A_{\text{IR}}(\tau)\hat{x}$] with the extreme ultraviolet (XUV)-IR delay $\tau_{\text{XUV-IR}}$ from the XUV pump pulse. The third term denotes the photoelectron excitation through the dipole transition by the \hat{x} -polarized XUV pulse [i.e., $A_{\text{XUV}}(\tau)\hat{x}$], where the matrix element M_{Lk} is

$$M_{Lk} = \int d^3r \psi_L^*(\mathbf{r}) \hat{x} \cdot \mathbf{k} \phi_{\mathbf{k}}(\mathbf{r}). \quad (2)$$

Radial functions of $2s$ and $2p_z$ states are obtained by the Hartree-Fock method [33]. Behaviors of $|M_{Lk}|^2$ are displayed in Fig. 1(c), where the Cooper minimum occurs around 70 eV for the $2s$ state and is known to generate exotic behaviors of emission delays [9,12,34]. Illustrations of p_x and d_{xz} photoelectron waves excited by the dipole operator from $2s$ and $2p_z$ states, respectively, are provided in Fig. 1(d). The pump

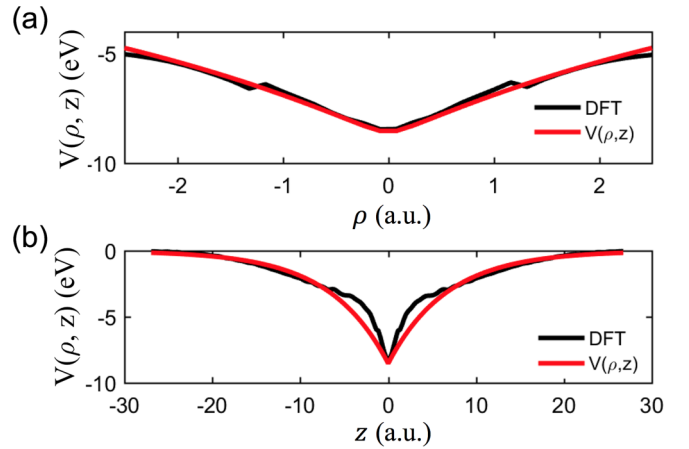


FIG. 2. Density fluctuation potential due to a created photohole from the DFT calculation (black) and $V(\rho, z)$ (red) of Eq. (4) with $\alpha = 0.25$ a.u. and $\beta = 0.15$ a.u. (a) $z = 0$ is taken. (b) $\rho = 0$ is taken.

and probe pulses are assumed to have Gaussian-cosine envelopes as depicted in Fig. 1(a). The probe pulse is assumed to have the frequency $\omega_{\text{IR}} = 1.5$ eV together with the amplitude $A_{\text{IR}}^0 = 0.05$ a.u. (a.u. is the atomic unit) and the half-width at half maxima (HWHM) 1.14 fs unless mentioned otherwise. On the other hand, the pump pulse should be the attosecond one with HWHM 400 as and its amplitude taken as $|A_{\text{XUV}}^0/A_{\text{IR}}^0| \simeq 10^{-6}$ for the whole calculation. The last term is the density fluctuation potential for a screening of the photohole, which plays a role of the scattering potential of the photoelectron

$$V_{\mathbf{k}\mathbf{k}'} = \int d^3r \phi_{\mathbf{k}}^*(\mathbf{r}) V(\mathbf{r}) \phi_{\mathbf{k}'}(\mathbf{r}), \quad (3)$$

in the plane-wave basis $\phi_{\mathbf{k}}(\mathbf{r})$. As we mentioned before, the potential should be anisotropic that it is reasonable to have a form of $V(\mathbf{r}) = V(\rho, z)$ with the cylindrical symmetry in a two-dimensional system. Meanwhile, it may be worthwhile to note that an approach using the model Hamiltonian of Eq.(1) could be shown to be quite successful in describing other localized systems (see Supplemental Figs. S2 and S3) [35].

To get the scattering potential $V(\mathbf{r})$, we use the DFT calculation by ELK [36]. For a 2×2 supercell, we obtain a difference in the potential between the ground state and the excited state with the photohole at a selected carbon atom, i.e., removing the $2s$ electron density in the corresponding muffin tin radius. The black lines in Figs. 2(a) and 2(b) show the anisotropic potential along in-plane and out-of-plane directions, respectively. Now we try a parametrization of the potential like

$$V(\rho, z) = V_0 e^{-\alpha\rho - \beta|z|}, \quad (4)$$

and fit the parameters to the DFT calculation of Fig. 2; α and β are screening parameters and their inverses correspond to the screening length along in-plane and out-of-plane directions. The screening parameters are taken as $\alpha = 0.25$ a.u. and $\beta = 0.15$ a.u. for the $2s$ photohole state of graphene, but found there is no meaningful difference between $2s$ and $2p_z$ photohole states. It should be noted that the photohole will be somewhat delocalized beyond a given muffin tin, which may

underestimate the potential depth. Additional simplifications may be enabled due to a feature of the single atomic layer of graphene. A photoelectron may have little chance of experiencing the crystal potential, which will be neglected here. Further, the initial state being taken as a core state, the density fluctuation due to a created photohole would induce quite a local screening, the Bloch characteristics and the multiple scattering would be limited.

The emission delay is obtained by solving the time-dependent Schrödinger equation $i\frac{\partial}{\partial\tau}|\psi(\tau)\rangle = \mathcal{H}|\psi(\tau)\rangle$, where $|\psi(\tau)\rangle$ is

$$|\psi(\tau)\rangle = a_L(\tau)|c_L\rangle + \sum_{\mathbf{k}} a_{\mathbf{k}}(\tau)|\mathbf{k}\rangle, \quad (5)$$

with $a_L(-\infty) = 1$. With the spherical \mathbf{k} -grid, we adopt the Runge-Kutta fourth-order algorithm to integrate the equation with an inherent cylindrical symmetry. In Supplemental Fig. S4 [35], a convergence of the calculation is demonstrated for the time step $\Delta\tau = 0.1$ a.u., the number of \mathbf{k} -point $(n_k, n_\theta, n_\phi) = (120, 18, 30)$, and the energy cutoff $E_{\max} = 400$ eV; θ and ϕ denote polar and azimuthal angles. From the time-dependent Schrödinger equation, we obtain a photoemission spectrogram with respect to the XUV-IR delay $\tau_{\text{XUV-IR}}$, and the photoelectron emission delay $\Delta\tau(\varepsilon_{\mathbf{k}}, \theta, \phi)$ for a selected momentum \mathbf{k} is extracted by measuring the time shift of the spectrogram [23,30].

III. RESULTS AND DISCUSSION

Our formulation makes it possible to obtain both angle-resolved and angle-integrated time delays under the anisotropic potential. Angle-integrated emission delays $\Delta\tau(\varepsilon_{\mathbf{k}})$ will be evaluated by

$$\Delta\tau(\varepsilon_{\mathbf{k}}) = \int_0^{2\pi} \int_0^\pi \Delta\tau(\varepsilon_{\mathbf{k}}, \theta, \phi) P(\theta, \phi) \sin\theta d\theta d\phi, \quad (6)$$

where $P(\theta, \phi)$ is the normalized probability for finding the photoelectron at given angles and $\Delta\tau(\varepsilon_{\mathbf{k}}, \theta, \phi)$ is the angle-resolved emission delay. Angle-integrated absolute delays for $2s$ and $2p_z$ states of graphene are provided with the photoelectron kinetic energy in Fig. 3(a). In the figure, the absolute delay could be compared with the case with $V(\mathbf{r}) = 0$ for each state, which is not actually measurable in the experiment. Instead, the relative delay between initial target states, say $\Delta\tau_{2p_z} - \Delta\tau_{2s}$ for a given photon energy is measured in an actual experiment. In the inset of Fig. 3(a), it can be seen that the $2s$ -originated photoelectron is emitted earlier than the $2p_z$ -originated photoelectron at given photon energies. This could be readily understood, especially for an isotropic system if the centrifugal barrier proportional to $l(l+1)$ is considered [2,11,24]. In an anisotropic system, however, the angular momentum contribution is a bit more complicated. The θ -dependent relative delay with ϕ integrated at a fixed photon energy $\omega_{\text{XUV}} = 48$ eV is displayed in Fig. 3(b). Near the normal emission ($\theta \lesssim 20^\circ$), the $2p_z$ -originated photoelectron is found to be emitted earlier. This is different from what is expected in the angle-integrated case, which implies that the angle dependence of the emission delay is in fact nontrivial. In Fig. 4, the angle-integrated emission delays for $2s$ and $2p_z$

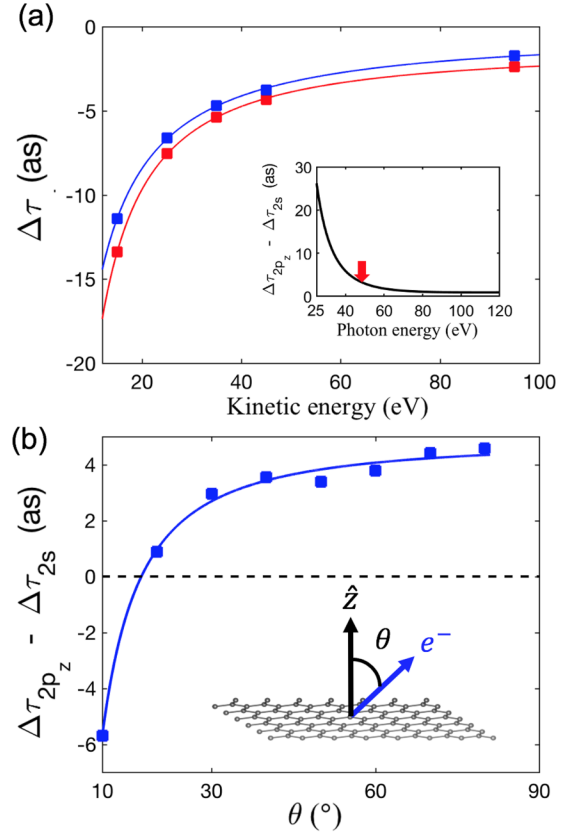


FIG. 3. (a) Angle-integrated absolute emission delay of $2s$ (red) and $2p_z$ (blue) photoelectron states. The inset shows the relative emission delay between $2s$ and $2p_z$ states, $\Delta\tau_{2p_z} - \Delta\tau_{2s}$. (b) Angle-resolved (with ϕ -integrated) relative emission delay with respect to θ at a given photon energy 48 eV [designated by a red arrow in the inset of (a)].

states are delivered for several values of anisotropic screening parameters of α and β .

Angle-dependent features in the absolute emission delay comes from two fundamental aspects. First, the photoelectron scattering potential of a two-dimensional system is characterized by anisotropic screening parameters α and β . In

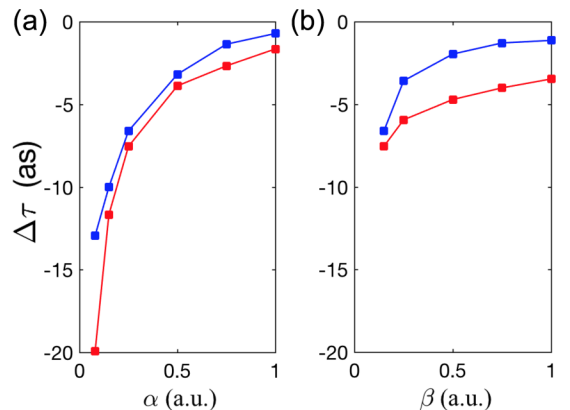


FIG. 4. Angle-integrated emission delay of $2s$ (red) and $2p_z$ (blue) states with respect to the screening parameters α and β at $\varepsilon_{\mathbf{k}} = 25$ eV. (a) $\beta = 0.15$ a.u. is fixed. (b) $\alpha = 0.25$ a.u. is fixed.

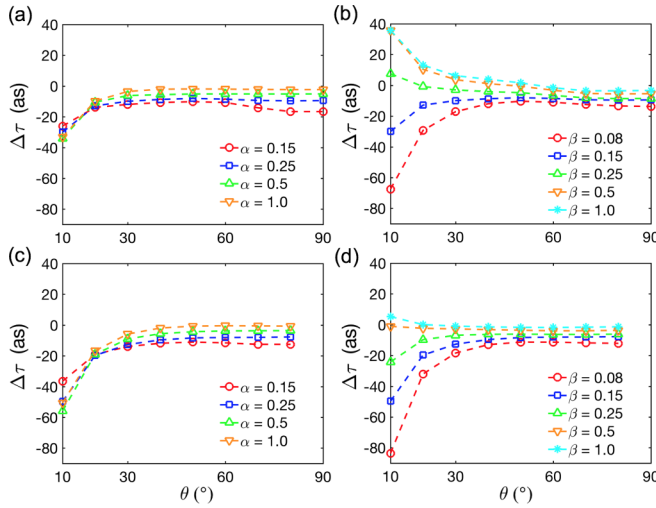


FIG. 5. Angle-resolved (with ϕ -integrated) emission delay $\Delta\tau$ at $\varepsilon_{\mathbf{k}} = 25$ eV for the screening parameters α and β . (a), (b) Photoelectron states from the $2s$ state. (c), (d) Photoelectron states from the $2p_z$ state. A variation of α (β) is considered for a fixed $\beta = 0.15$ a.u. ($\alpha = 0.25$ a.u.). Note that the data at 90° in (c) and (d) are removed because the corresponding cross-section is almost zero (see Supplemental Fig. S6 [35]).

Fig. 5, it is reasonably shown that in-plane and out-of-plane screening parameters α and β have strong effects on the time delays of the electron emitted along grazing ($\theta \rightarrow 90^\circ$) and normal ($\theta \rightarrow 0$) directions, respectively. Nevertheless, some cross couplings between the screening parameter and the anisotropic delay are still observed, which would be caused by the off-diagonal scattering due to $V_{\mathbf{k}\mathbf{k}'}$. That is, the intermediate states which experience the scattering contribute to the final angle-dependent emission delay. Additionally, there is a change of the angular momentum brought about by the anisotropic potential. When a photoelectron is scattered by the cylindrical symmetric potential, the orbital quantum number l is not a good quantum number any more. Thus the potential scattering generates a linear combination of all possible l states, for instance, the p_x wave emitted from the $2s$ state would change to the d_{xz} wave particularly at small α (see Figs. S5 and S6) [35]. Second, the IR-induced continuum transition and the Fano propensity rule lead to the angle dependence of the emission delay [29].

According to Figs. 5(a) and 5(c), the in-plane parameter α dominantly influences the emission delay near along the grazing direction, but the angle dependence is not so substantial. On the other hand, Figs. 5(b) and 5(d) indicate that the strong angle dependence of the emission delay near along the normal direction is developed by the out-of-plane parameter β . In particular, for $\beta \gtrsim 0.25$ a.u. (the $2s$ state) or $\beta \gtrsim 0.5$ a.u. (the $2p_z$ state) at a fixed $\alpha = 0.25$ a.u., even a sign change in the emission delay is attained at small angles of θ . A positive delay implies a retardation of the electron emission, i.e., later electron emission, compared to a case with $V(\mathbf{r}) = 0$. It is actually puzzling to have a positive absolute delay under the attractive localized potential because a negative delay is generally expected due to an increase of the photoelectron kinetic energy compared to the free space [24].

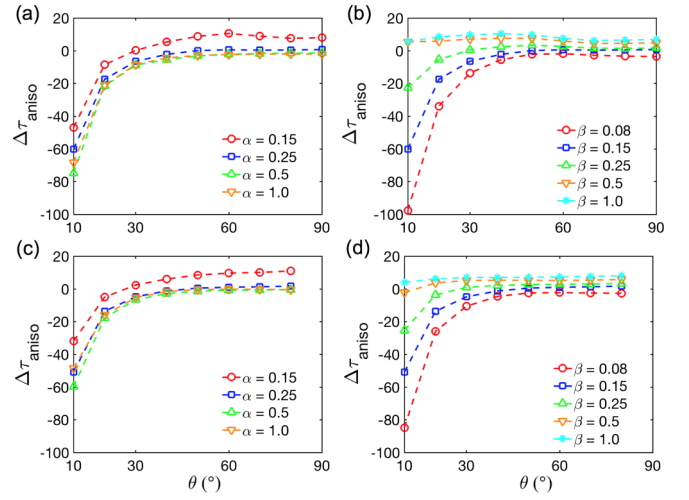


FIG. 6. Angle-resolved (with ϕ -integrated) emission delay $\Delta\tau_{\text{aniso}}$ with the anisotropic potential effects isolated, i.e., $\Delta\tau_{\text{aniso}} = \Delta\tau - \Delta\tau_{\text{iso}}$ at $\varepsilon_{\mathbf{k}} = 25$ eV for the screening parameters α and β . (a), (b) Photoelectron states from the $2s$ state. (c), (d) Photoelectron states from the $2p_z$ state. A variation of α (β) is considered for a fixed $\beta = 0.15$ a.u. ($\alpha = 0.25$ a.u.).

To get an insight about that, we calculate the absolute emission delay $\Delta\tau_{\text{iso}}$ for an isotropic scattering potential $V(\mathbf{r}) = V_0 e^{-\alpha r}$ by solving the time-dependent Schrödinger equation, exactly on an equal footing with the previous. A possible angle dependence of $\Delta\tau_{\text{iso}}$ could be regarded as the contribution from the IR-induced continuum transition. We then define the emission delay $\Delta\tau_{\text{aniso}}$ by isolating the sole contribution of the anisotropic potential, that is, by subtracting $\Delta\tau_{\text{iso}}$ from $\Delta\tau$, just like $\Delta\tau_{\text{aniso}} = \Delta\tau - \Delta\tau_{\text{iso}}$. In Figs. 6(a) and 6(c), α is found to make constant gains in the emission delays $\Delta\tau_{\text{iso}}$ so that its variation can hardly induce noticeable changes in the angle dependence of the delays. In contrast, Figs. 6(b) and 6(d) are more insightful. Intriguing positive delays near along the normal direction in $\Delta\tau$ of Figs. 5(b) and 5(d) are almost removed in $\Delta\tau_{\text{aniso}}$ of Figs. 6(b) and 6(d). This indicates that $\Delta\tau_{\text{iso}}$ decisively contributes to positive delays at small angles of θ , which should be from the IR-induced continuum transition. Consequently, as demonstrated in Figs. 6(b) and 6(d), the conical electron emission with appreciable negative delays at $\theta \lesssim \theta_c$ would be manifested, especially at $\beta \ll \alpha$, where θ_c may be defined as a critical angle. At θ smaller than θ_c , the emission delay becomes appreciably negative. Last, it may be worthwhile to comment on the quantum interference occurring in the photoemission streaking under the anisotropic scattering potential. When β is small (i.e., compared to α), the anisotropic potential produces a mixing of all possible angular momentum states. Those states would interfere with each other in a complicated way [29] and then eventually deliver $\Delta\tau_{\text{aniso}}$ driving a velocity cone of earlier electron emission as given in Fig. 6.

IV. SUMMARY AND CONCLUSION

In conclusion, we have calculated the angle-resolved photoelectron emission delay in a two-dimensional arrangement of carbon atoms, i.e., graphene by solving the time-dependent

Schrödinger equation under the model Hamiltonian accompanying the anisotropic scattering potential. The anisotropic potential has been acquired from the DFT calculation and further parameterized for an extensive analysis. From our calculation, it is found that the absolute emission delays of $2s$ and $2p_z$ states of graphene show the strong angle dependencies derived from the IR-induced continuum transition and the anisotropic scattering potential. The effect of the sole anisotropic potential could be isolated by comparing with a case with the isotropic potential, which should correspond to the quantum interference by a mixing of the angular momen-

tum states. This is found to drive a velocity cone of earlier electron emission centering around the direction normal to the atomic layer.

ACKNOWLEDGMENTS

This work was supported by the Basic Science Research Program (2019R1A2C1005050) through the National Research Foundation of Korea (NRF) and also by the DGIST R&D program (21-CoE-NT-01), supported by the Ministry of Science and ICT.

-
- [1] A. L. Cavalieri, N. Müller, T. Uphues, V. S. Yakovlev, A. Baltuška, B. Horvath, B. Schmidt, L. Blümel, R. Holzwarth, S. Hendel, M. Drescher, U. Kleineberg, P. M. Echenique, R. Kienberger, F. Krausz, and U. Heinzmann, *Nature* **449**, 1029 (2007).
- [2] M. Schultze, M. Fieß, N. Karpowicz, J. Gagnon, M. Korbman, M. Hofstetter, S. Neppl, A. L. Cavalieri, Y. Komninos, T. Mercouris, C. A. Nicolaides, R. Pazourek, S. Nagele, J. Feist, J. Burgdörfer, A. M. Azzeer, R. Ernstorfer, R. Kienberger, U. Kleineberg, E. Goulielmakis *et al.*, *Science* **328**, 1658 (2010).
- [3] L. Eisenbud, Ph.D. thesis, Princeton University, 1948.
- [4] E. P. Wigner, *Phys. Rev.* **98**, 145 (1955).
- [5] F. T. Smith, *Phys. Rev.* **118**, 349 (1960).
- [6] A. S. Kheifets and I. A. Ivanov, *Phys. Rev. Lett.* **105**, 233002 (2010).
- [7] J. M. Dahlström, D. Guénot, K. Klünder, M. Gisselbrecht, J. Mauritsson, A. L'Huillier, A. Maquet, and R. Taïeb, *Chem. Phys.* **414**, 53 (2013).
- [8] R. Pazourek, J. Feist, S. Nagele, and J. Burgdörfer, *Phys. Rev. Lett.* **108**, 163001 (2012).
- [9] P. C. Deshmukh, A. Mandal, S. Saha, A. S. Kheifets, V. K. Dolmatov, and S. T. Manson, *Phys. Rev. A* **89**, 053424 (2014).
- [10] M. Ossiander, F. Siegrist, V. Shirvanyan, R. Pazourek, A. Sommer, T. Latka, A. Guggenmos, S. Nagele, J. Feist, J. Burgdörfer, R. Kienberger, and M. Schultze, *Nat. Phys.* **13**, 280 (2017).
- [11] M. Isinger, R. Squibb, D. Busto, S. Zhong, A. Harth, D. Kroon, S. Nandi, C. Arnold, M. Miranda, J. M. Dahlström, E. Lindroth, R. Feifel, M. Gisselbrecht, and A. L'Huillier, *Science* **358**, 893 (2017).
- [12] D. Hammerland, P. Zhang, A. Bray, C. Perry, S. Kuehn, P. Jojart, I. Seres, V. Zuba, Z. Varallyay, K. Osvay, A. Kheifets, T. T. Luu, and H. J. Wörner, *arXiv:1907.01219* (2019).
- [13] J. M. Dahlström and E. Lindroth, *J. Phys. B: At. Mol. Opt. Phys.* **49**, 209501 (2016).
- [14] P. C. Deshmukh, A. Kumar, H. R. Varma, S. Banerjee, S. T. Manson, V. K. Dolmatov, and A. S. Kheifets, *J. Phys. B: At. Mol. Opt. Phys.* **51**, 065008 (2018).
- [15] F. Siek, S. Neb, P. Bartz, M. Hensen, C. Strüber, S. Fiechter, M. Torrent-Sucarrat, V. M. Silkin, E. E. Krasovskii, N. M. Kabachnik, S. Fritzsche, R. D. Muiño, P. M. Echenique, A. K. Kazansky, N. Müller, W. Pfeiffer, and U. Heinzmann, *Science* **357**, 1274 (2017).
- [16] R. O. Kuzian and E. E. Krasovskii, *Phys. Rev. B* **102**, 115116 (2020).
- [17] Q. Liao and U. Thumm, *Phys. Rev. Lett.* **112**, 023602 (2014).
- [18] C. Lemell, S. Neppl, G. Wachter, K. Tókési, R. Ernstorfer, P. Feulner, R. Kienberger, and J. Burgdörfer, *Phys. Rev. B* **91**, 241101(R) (2015).
- [19] S. A. Sato, H. Hübener, A. Rubio, and U. De Giovannini, *Eur. J. Phys.* **91**, 126 (2018).
- [20] M. Volkov, S. A. Sato, F. Schlaepfer, L. Kasmi, N. Hartmann, M. Lucchini, L. Gallmann, A. Rubio, and U. Keller, *Nat. Phys.* **15**, 1145 (2019).
- [21] G. Bae, H. Park, and J. D. Lee, *Phys. Rev. B* **103**, 165413 (2021).
- [22] M. Fanciulli, H. Volfová, S. Muff, J. Braun, H. Ebert, J. Minár, U. Heinzmann, and J. H. Dil, *Phys. Rev. Lett.* **118**, 067402 (2017).
- [23] J. D. Lee, *Phys. Rev. B* **86**, 035101 (2012).
- [24] J. M. Dahlström, A. L'Huillier, and A. Maquet, *J. Phys. B: At. Mol. Opt. Phys.* **45**, 183001 (2012).
- [25] R. Pazourek, S. Nagele, and J. Burgdörfer, *Rev. Mod. Phys.* **87**, 765 (2015).
- [26] S. Heuser, Á. J. Galán, C. Cirelli, C. Marante, M. Sabbar, R. Boge, M. Lucchini, L. Gallmann, I. Ivanov, A. S. Kheifets, J. M. Dahlström, E. Lindroth, L. Argenti, F. Martín and U. Keller, *Phys. Rev. A* **94**, 063409 (2016).
- [27] V. V. Serov and A. Kheifets, *Phys. Rev. A* **93**, 063417 (2016).
- [28] A. W. Bray, F. Naseem, and A. S. Kheifets, *Phys. Rev. A* **97**, 063404 (2018).
- [29] D. Busto, J. Vinbladh, S. Zhong, M. Isinger, S. Nandi, S. Maclot, P. Johnsson, M. Gisselbrecht, A. L'Huillier, E. Lindroth and J. M. Dahlström, *Phys. Rev. Lett.* **123**, 133201 (2019).
- [30] J. D. Lee, *Phys. Rev. Lett.* **111**, 027401 (2013).
- [31] G. D. Mahan, *Many-Particle Physics* (Springer Science & Business Media, 2013).
- [32] S. Korschuh, M. Gmitra, and J. Fabian, *Phys. Rev. B* **82**, 245412 (2010).
- [33] D. T. Waide, D. G. Green, and G. F. Gribakin, *Comput. Phys. Commun.* **250**, 107112 (2020).

- [34] C. Cirelli, C. Marante, S. Heuser, C. Petersson, J. Galán, L. Argenti, S. Zhong, D. Busto, M. Isinger, S. Nandi, S. Maclot, L. Rading, P. Johnsson, M. Gisselbrecht, M. Lucchini, L. Gallmann, J. M. Dahlström, E. Lindroth, A. L'Huillier, F. Martín, and U. Keller, *Nat. Commun.* **9**, 955 (2018).
- [35] See Supplemental Material at <http://link.aps.org/supplemental/10.1103/PhysRevB.103.235135> for details of model derivation, example calculations, and supporting data, which includes Ref. [37].
- [36] See <http://elk.sourceforge.net>.
- [37] S. Nagele, R. Pazourek, J. Feist, K. Doblhoff-Dier, C. Lemell, K. Tórkési, and J. Burgdörfer, *J. Phys. B: At. Mol. Opt. Phys.* **44**, 081001 (2011).